Corrigenda to The Proceedings of SAIP2021, the 65th Annual Conference of the South African Institute Of Physics, ISBN: 978-0-620-97693-0

Effect of Gold Nanoparticle-Hypericin Mediated Photodynamic Therapy in MCF-7 Breast Cancer Cells.

DR Mokoena[1], BP George[1] and H Abrahamse[1,2]

[1]Laser Research Centre, Faculty of Health Sciences, University of Johannesburg, P.O. Box: 17011, Johannesburg 2028, South Africa
[2]NRF SARChI: Laser Applications in Health, South Africa

E-mail: habrahamse@uj.ac.za

Abstract. Cancer is a global emergency that needs instant intervention. Breast cancer is the second most common cancer after lung and the most common cancer amongst women. Current treatments are linked with adverse side effects, treatment failure, and cancer relapse. Photodynamic therapy (PDT) is one of the emerging cancer treatment options that is highly selective and specific towards cancer cells. Consequently, the use of gold nanoparticles (AuNP) further enhances the efficacy of PDT. In this study, gold-nanoparticle (AuNP) conjugated Hypericin (Hyp) mediated PDT was used for the treatment of MCF-7 human breast cancer cells by inducing cell death, *in vitro*. Cellular responses after 24 h post-PDT, and at 10 J/cm^2 were observed. The morphological changes, viability, cytotoxicity, and cell death mechanism analysis by Annexin V/PI staining was performed. The results showed activation of the apoptotic pathway with characteristic morphological features and biochemical responses of dying cells. Hence this study provided an insight into the application of advanced PDT in breast cancer treatment by actively targeting the apoptotic cell death pathway *in vitro*.

1. Introduction

Breast cancer begins when there is an uncontrolled growth of breast cells, leading to lump formation, inflammation, and metastasis to other parts of the body. Several different types of breast cancers have been identified. Such as those that begin from the ducts of the breast referred to as ductal carcinoma in situ or the ones that are in the lobules of the breast known as lobular carcinoma in situ [1]. Another uncommon yet increasing form of breast cancer is inflammatory breast cancer which is characterized by the warm, red, and swollen appearance of the breast. Breast cancer is a heterogeneous disease, and its treatment varies depending on the location of the tumour and whether it is benign or malignant. Current treatments are associated with several undesirable side effects such as poor prognosis, poor survival rate, drug resistance, and cytotoxicity to normal cells resulting in poor quality of life. In Africa, the five-year survival rate is less or equal to 60% for low and middle-income countries [2].

Photodynamic therapy (PDT) is a novel therapy due to its selective cytotoxicity and much reduced invasive quality [3]. It utilizes the use of a Photosensitiser (PS), visible light at a specific wavelength, as well as molecular oxygen to abolish cancer cells and disease causing bacteria [4]. It has the potential to meaningfully improve the quality of life and lengthen the survival rates in cancer patients. In PDT the PS plays a vital role in cancer cell destruction by entering the cell and activation with a specific wavelength light. Some PSs like hypericin, are hydrophobic and require a carrier molecule such as nanoparticles to enter the cell. Thus, increasing their movement across the cell membranes as a result of

increased aqueous solubility, stability, and bioavailability [5, 6]. PS and nanoparticle conjugates have proven to improve PDT efficiency. Using gold nanoparticles Portilho et al., 2013 observed an increased triplet lifetime of PS than unconjugated PS [7]. Some studies have demonstrated increased PS drug delivery and preservation using nanoparticles [8]. Nanoparticles have also been observed to disguising the PS from biological barricades and enzymes, resulting in improved cellular uptake with augmented ROS synthesis [9].

2. Materials and Methods

Hypericin (Sigma-Aldrich, 1MG-56690) was prepared in Dimethyl sulfoxide (DMSO), to a final stock concentration of 0.02 M. It was then conjugated with gold nanoparticles (AuNPs) (Sigma-Aldrich, 1ML-765457) by sonication for 2 h at room temperature. UV-Vis Spectrophotometry was used to determine the activation wavelength of Hypericin, AuNP, and the conjugate from 200 – 800 nm wavelengths. Dynamic Light Scattering (DLS), Zeta potential, and Fourier-transform infrared (FTIR) spectroscopy were used to characterize the conjugate. MCF-7 Breast cancer cells were commercially purchased from the ATCC, (ATCC® HTB-22™) and seeded in Dulbecco's Modified Eagle's Medium (DMEM) supplemented with 10% Foetal Bovine Serum, 1% amphotericin B, 1% pen-strep and incubated at 37 °C, 85% humidity and 5% CO_2. For PDT experiments, 3×10^5 cells were seeded in 3.4 cm^2 cell culture plates and treated with Hypericin-AuNP conjugate at concentrations of 3.8, 7.6, and 15.2 μM per plate. After 12 h of incubation to allow maximum absorption of the PS by the cells, the cells were washed 3 times using pre-warmed Hank's Balanced Salt Solution (HBSS) to eliminate unabsorbed PS. The treated cells were then irradiated using a 594 nm diode laser (Oriel Corporation), supplied by the National Laser Center (NLC) of South Africa. Cells were irradiated at a fluence of 10 J/cm^2 as shown in table 1 below.

Table 1. Laser Parameters for PDT

Variable	Value/Description
Wavelength	594 nm
Laser type	Diode laser
Wave release	Continuous wave
Energy density	10 J/cm^2
Power output	91.1 mW
Power density	10 mW/cm^2
Spot size	9.1 cm^2
Irradiation time	16 min 42 sec

Following irradiation, cells were placed in the incubator for 24h and the morphology was checked using an inverted light microscope (Wirsam, Olympus CKX41). The cell proliferation assay was done using the CellTiter-Glo Luminescence Cell Viability Assay (Promega, G7570) to check the amount of ATP present in the cells. The luminescence signal produced from the conversion of ATP to adenosine monophosphate (AMP) by the enzyme luciferase was read out in relative light units (RLU) on the Victor-3 multi-plate reader ((Perkin Elmer, VICTOR Nivo Multimode Microplate Reader). The signal is directly proportional to the amount of ATP in the cells, which represents the number of metabolically active cells. Cellular cytotoxicity was analyzed using the spectrophotometric analysis of Lactate Dehydrogenase, LDH at 490 nm ((Perkin Elmer, VICTOR Nivo Multimode Microplate Reader). The CytoTox 96® Non-Radioactive Cytotoxicity Assay (Anatech: Promega, PRG1780) was utilized to detect the amount of LDH in the media. Annexin V- fluorescein isothiocyanate (FITC) apoptosis detection kit1 (BD Biosciences, BD Pharmingen™) was used to analyze the apoptotic or necrotic cell death pathways and the flow cytometric analysis was performed using the BD Accuri C6 (BD

Biosciences). All experiments were repeated three-times (n=3). The SSPS software version 27 was used for statistical analysis. Dunnett with a Confidence interval of 0.95% was used between the control (cells only) and experimental groups at significance levels $p< 0.05$ (*), $p< 0.01$ (**) and $p<0.001$(***).

3. Results

The results indicated damage to Hyp-AuNP PDT treated cells compared to the untreated control cells. The morphology images (Figure 1) distinctly show the rounding up of cells and detachment from the culture dish surface. The higher the concentration of the conjugate, more number of cells showed rounding up, detachment from the culture dish, and thus cell death in PDT treated cells. Cellular responses also showed a dose-dependent cell death. LDH levels were increased with the increasing concentration of conjugate ($p<0.01$) in experimental PDT groups (3.8, 7.6 and 15.2 µM at 10 J/cm^2) (Figure 2) while ATP levels decreased when compared to the untreated cells ($p<0.05$). There was no significant difference when control cells were compared to the Hyp-AuNP conjugate only treated group (Figure 3). The Annexin V/PI flow cytometry results (Figure 4) indicate the early and late apoptotic cell death after the treatments.

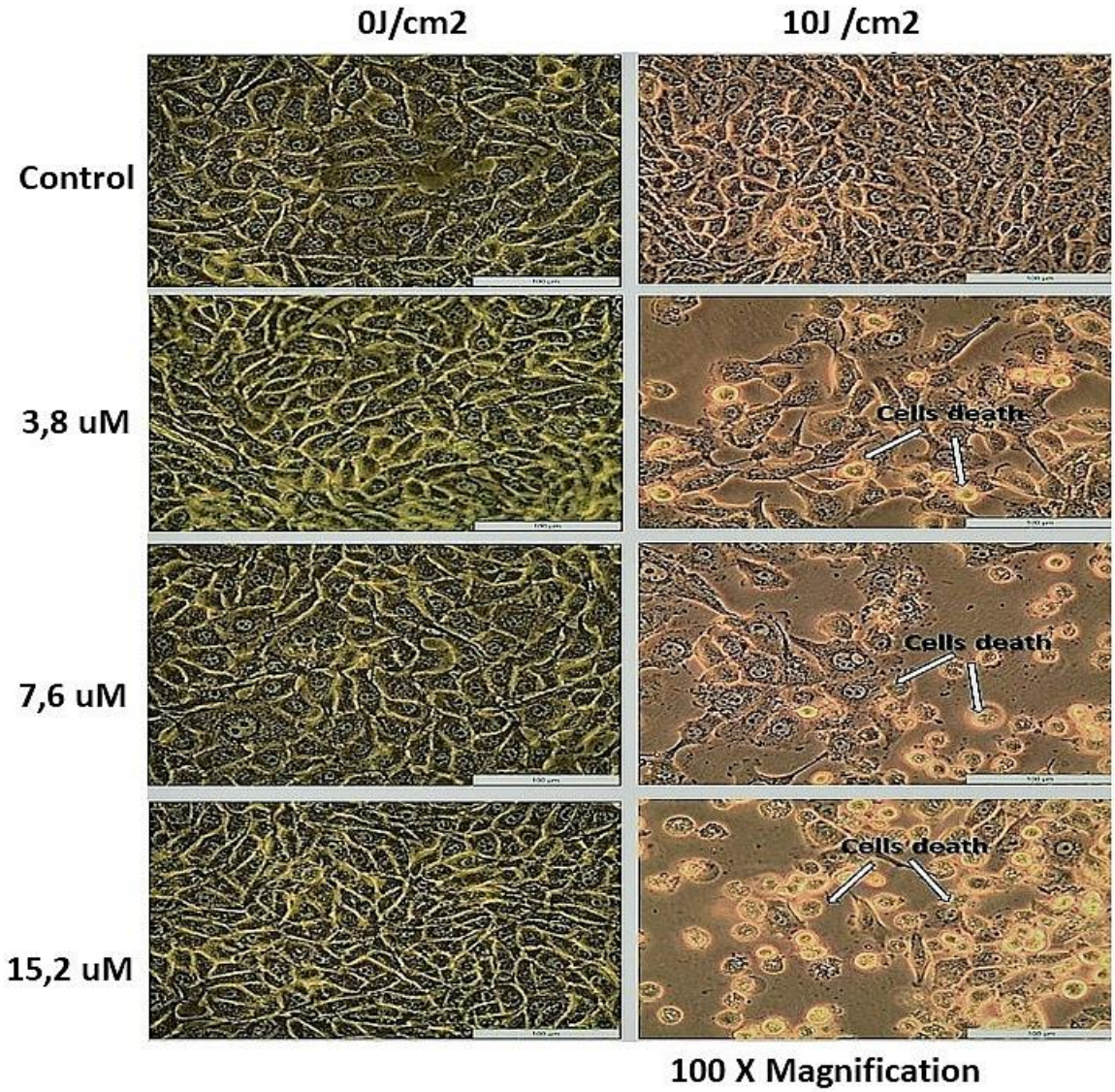

Figure 1. Morphology of MCF-7 cells pre- and post-PDT at 594 nm.

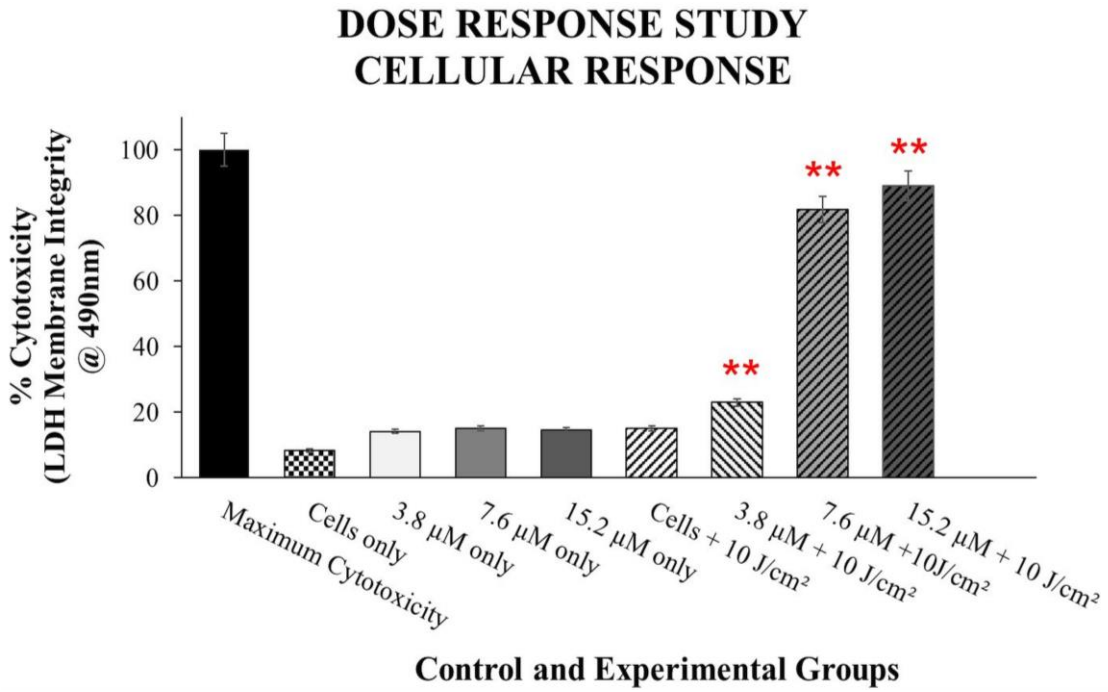

Figure 2. Lactate dehydrogenase hydrogenase (LDH) cytotoxicity assay indicated a significant (p<0.01) ** increase in LDH levels in Hyp-AuNP PDT treated cells compared to the control cells.

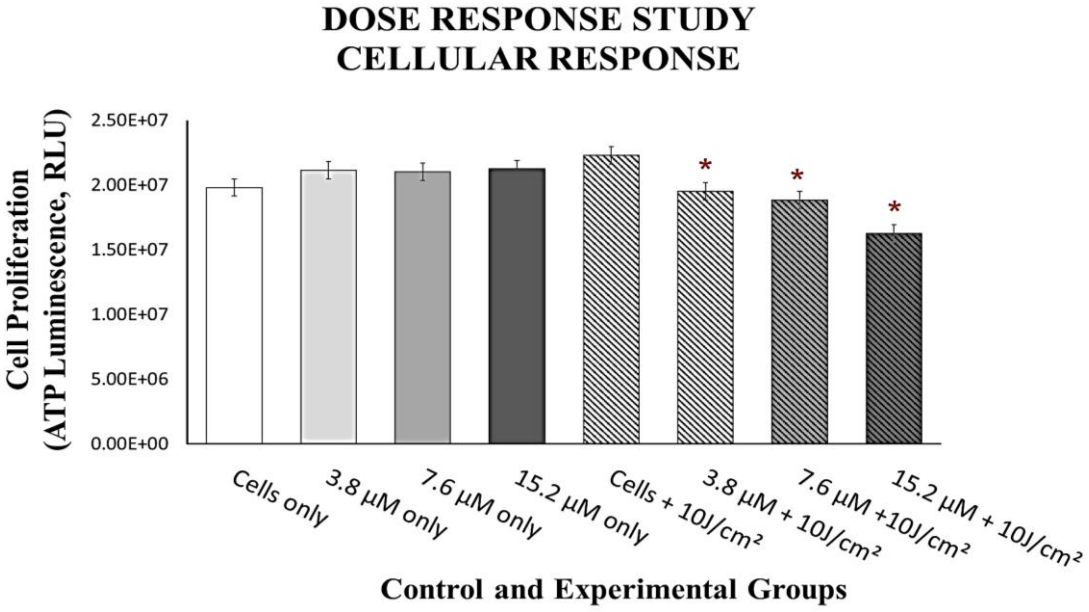

Figure 3. ATP Luminescence of cells indicating the rate of proliferation. Control cells in comparison to PDT treated groups showed a significant (p<0.05)* decrease in ATP proliferation after 24 h. No significance was observed when control cells were compared with groups that only received the Hyp-AuNP conjugate.

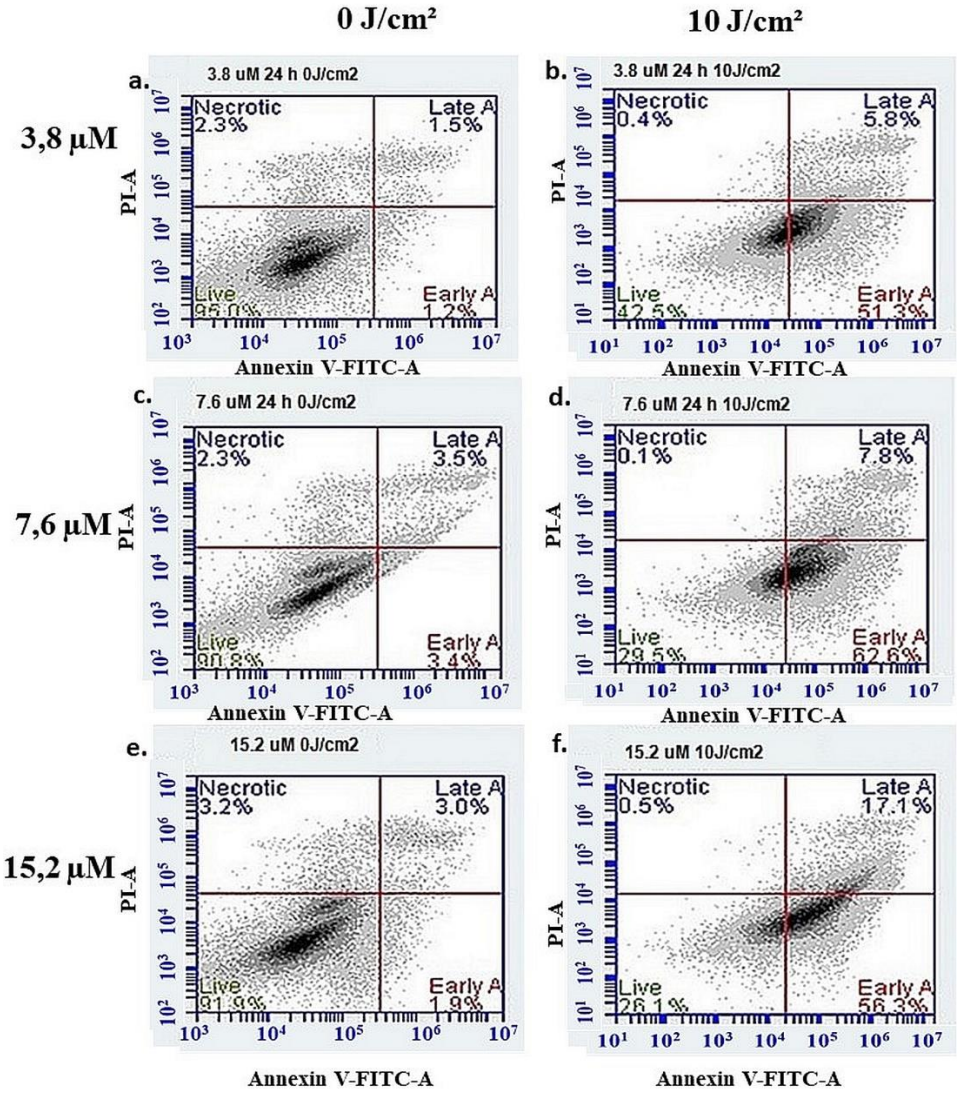

Figure 4. Annexin V/PI Flow cytometry results demonstrating early and late stage apoptosis at 24h post irradiation, where early apoptosis is shown as a percentage of the total population in the lower right quadrant and late-stage apoptosis shown as a percentage in the upper right quadrant. Plots a, c and e are non-irradiated control groups, while plots b, d and f are the PDT treated experimental groups.

4. Discussion and Conclusion

PDT prompts cell death by the production of reactive oxygen species resulting in oxidative damage to the cells, which results in cell death via apoptosis, necrosis, or autophagy [10]. In this study, the varying concentrations of the nano-PS conjugate resulted in significant photodamage to cells following laser irradiation at 594 nm. The morphology of conjugate PDT treated cells showed distinct damage compared to the untreated cells. This was further confirmed by the significantly decreased levels of ATP in proliferation assay results which indicated the decrease in cell proliferation in comparison to the cells only and cells treated with the nano-conjugate alone. There was an increase in the LDH levels in treated cells as compared to the untreated cells this indicates the damage to the cell membrane in treated cells following PDT and incubation at 24 h. The Annexin V/PI results indicate the oxidative cell damage in treated cells was due to the induction of early and late apoptosis.

Several studies have demonstrated the effects of Hypericin in PDT [11, 12]. However, its hydrophobicity has always been an issue, leading to the reduced cellular uptake and localization due to reduced movement through the cellular membrane of cancer cells. Conjugation of Hypericin to nanoparticles proves to be more effective and leading to an enhanced PDT efficacy than when used alone [13]. Hyp-AuNPs conjugate has demonstrated the desired therapeutic effects in MCF-7 cells in *in-vitro*. However, more studies need to be performed on normal breast cells to ensure the specificity of the treatment with no side effects to normal cells.

Acknowledgments
This work is based on the research supported by the South African Research Chairs Initiative of the Department of Science and Technology and the National Research Foundation of South Africa (Grant No 98337). The authors sincerely thank the University of Johannesburg, the National Research Foundation for their financial grant support, and the National Laser Centre for providing use of their lasers

References

[1] What Is Breast Cancer? | Breast Cancer Definition [Internet]. [cited 2021 Aug 26]. Available from: https://www.cancer.org/cancer/breast-cancer/about/what-is-breast-cancer.html
[2] Vanderpuye V, Grover S, Hammad N, PoojaPrabhakar, Simonds H, Olopade F, et al. 2017. *Infect. Agents Cancer* **12** 13.
[3] Agostinis P, Berg K, Cengel KA, Foster TH, Girotti AW, Gollnick SO, et al. 2011 CA*Cancer J Clin* **61** 250–81.
[4] Abrahamse H and Hamblin MR 2016 *Biochem J* **473** 347–64.
[5] Jia X and Jia L 2012 *Curr Drug Metab* **13** 1119–22.
[6] Plenagl N, Duse L, Seitz BS, Goergen N, Pinnapireddy SR, Jedelska J, et al. 2019 *Drug Deliv* **26** 23–33.
[7] Portilho FA, Cavalcanti CE deOliveira, Miranda-Vilela AL, Estevanato LLC, Longo JPF, Almeida Santos M deFátimaMenezes, et al. 2013 *J Nanobiotechnol* **11** 41.
[8] Stuchinskaya T, Moreno M, Cook MJ, Edwards DR and Russell DA 2011 *Photochem Photobiol Sci* **10** 822–31.
[9] Zhu J, Zheng L, Wen S, Tang Y, Shen M, Zhang G, et al. 2014 *Biomaterials* **35** 7635–46.
[10] Kubiak M, Łysenko L, Gerber H and Nowak R 2016 *Postepy Hig Med Dosw* **70** 735–42.
[11] Kiro N and Abrahamse H (MCF-7). *SAIP Proceeding*:5.
[12] Ali SM and Olivo M 2002 *Int J Oncol* **21** 531–40.
[13] Yermak PV, Gamaleia NF, Shalamay AS, Saienko TV and Kholin VV 2010 *Exp Oncol* **4**.

Comparison of Indoor Radon Levels measured with three different Detectors (Passive and Active)

C G Sethabela[1], A R Ocwelwang[1, 2], M Mathuthu[1] and A M Maheso[3]
[1]Centre for Applied Radiation Science and Technology, North-West University Mahikeng Campus, Corner of Albert Luthuli and University Drive Mmabatho. Private Bag X2046 Mmabatho, 2745.
[2]Centre for Nuclear Safety and Security (CNSS), National Nuclear Regulator (NNR), Eco Glades 2 Block G, 420 Witch Hazel Avenue, Highveld, Centurion. PO Box 7106 Centurion, 0046.
[3]Department of Physics, University of Stellenbosch-49 Victoria Street, Stellenbosch. Private Bag X1, Matieland 7602, South Africa.

E-mail: csethabela@gmail.com

Abstract. Radon is a non-reactive, naturally occurring gas that emanates during the decay of uranium-238 (^{238}U) to radium-226 (^{226}Ra) then radon-222 (^{222}Rn). This radioactive gas is colourless, odourless and invisible. It is present in air, soil, water and building materials. Radon gas can be measured using two different measurement techniques, active and passive techniques.In this study, three types of radon detectors were deployed in two rooms at CARST to measure the indoor radon concentration. The detectors used were the AlphaGUARD model PQ 2000 detector, Airthings wave monitor and Solid-State Nuclear Track Detector (SSNTD). The detectors were deployed for three months. Results from the waste room showed that the SSNTD measured a radon concentration of 77±13 Bq/m^3. The AlphaGUARD and Airthings monitors recorded an average radon concentration of 37±10 Bq/m^3 and 35±18 Bq/m^3, respectively. Results from the CARST office showed that the SSNTD measured a radon concentration of 68±12 Bq/m^3. The AlphaGUARD and Airthings monitors recorded an average radon concentration of 19±11 Bq/m^3 and 12±3 Bq/m^3, respectively. The average radon levels obtained from the Airthings wave plus monitor and the AlphaGUARDare within a close range compared to the passive SSTND results. However, results from all measurement techniques did not display alarming levels as they are below the recommended World Health Organization (WHO) national reference level of 100 Bq/m^3.

1. Introduction

Radon (^{222}Rn) is a chemically inert, radioactive gas that occurs naturally in the earth's crust. This gas has a half-life of 3.8 days. It is colourless, odourless and tasteless, and it tends to accumulate to high concentration levels inside buildings [1]. Radon emanates from the radioactive decay series of uranium-238 (^{238}U). It is formed by the emission of an alpha particle from its parent radionuclide radium-226 (^{226}Ra). Radon is also an alpha emitter; it emits alpha particles when it decays to its progeny, polonium-218 (^{218}Po) and polonium-

214 (^{214}Po) [1]. Sources of indoor radon include soil, rocks, and groundwater. Radon accumulates in buildings by moving from soil and rocks into the air and seeping into buildings by advection and diffusion. Buildings without airbricks or ventilation systems and buildings with cracksare more at risk of high radon accumulation [2, 3].

Studies have shown that building materials can also be a source of indoor radon if they contain certain radioactive elements, including uranium [4]. Meteorological factors such as temperature, air pressure, and humidity have also influenced indoor radon levels. Radon has been listed as the second leading cause of lung cancer by International Agency for Research on Cancer (IARC) [5]. Thus, knowing the level of ionising radiation and indoor radioactivity in buildings where people spend most of their time is of great importance; this includes homes and workplaces such as schools, universities and offices.

1.1. Description of the study area

The Centre for Applied Radiation Science and Technology (CARST) is one of the North-West University Mafikeng Campus departments under the Natural and Agricultural Sciences faculty. The CARST facilities consist of three buildings, and measurements were taken in two of these buildings, the lecturer's office and the waste room. The two rooms are built with the same type of building materials and floor type. Ventilation in these rooms is different; the office has a window. It is frequently opened and occupied during the week but closed over weekends. The waste room does not have a window but a door that is closed 90% of the time. This door is opened only when there is an activity in the waste room.

The radioactive waste room stores low-level radioactive waste, mainly from environmental samples, like soil, water, rock and plants. There are also beakers, gloves and paper towels used by the researchers and students in the facility. All these materials were used for research. Samples stored in this room are collected from mine dams and waste rocks, Tailing Facilities Storage (TFS) and areas near mines. The lack of ventilation in the waste room makes the waste room and ultimately the laboratory conducive for radon gas accumulation. It is thus essential to measure and monitor the 222Rn concentration levels in this waste room. Due to the risks associated with exposure to ionising radiation, radioactive waste materials cannot be disposed of as regular waste. Standard procedures need to be followed according to the type of waste (high level, medium level and low-level radioactive waste) classified by the IAEA and regulated by the NNR. Therefore, every facility that generates radioactive waste should follow regulatory procedures to effectively isolate, store, and dispose of waste [6]. According to the WHO, measuring and monitoring 222Rn in dwellings and public buildings is the most effective way to protect people from potential health risks [7].

2. Method and Material

2.1. Description of instruments used

Many detectors are used to measure radon concentration; detectors used are either passive or active techniques. They can detect alpha particles emitted when ^{222}Rn decay to its progenies. Each method is best depending on the application. Integrative, passive radon detectors do not require electrical power to operate, while continuous active radon detectors require electrical power [8]. This study employed three different detectors to measure indoor radon concentration. The solid-state nuclear track detector (SSNTD), also called "etched track detector", is a passive technique. The AlphaGUARD and Airthings Waves radon detectors are active techniques.

2.1.1. Integrated Passive Radon Detector: Solid-State Nuclear Track Detectors (SSNTD). Figure 1 displays the SSNTD that was used in this study. The SSNTD comprises a thin plastic film (Figure 2) of materials capable of recording alpha tracks emitted by radon and its progenies. Track detectors exist in open and closed types, and sampling is done in passive mode. The plastic film usually comes in two types, the LR115 (cellulose nitrate) and CR-39 (polyallyl diglycol carbonate). After exposure of the detector for a specified period, the plastic material is etched in NaOH or KOH solution to reveal any track damages (Figure 2). The exposure period is usually long enough to get representative data [9].

Figure 1. PARC RGM Solid State Nuclear Track Detector [10].

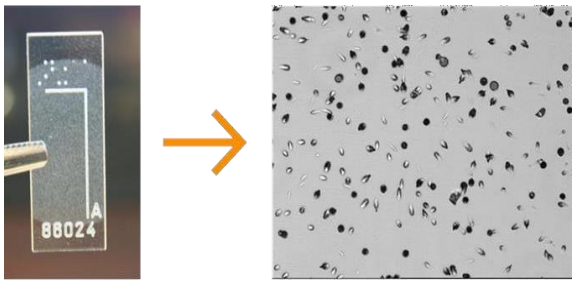

Figure 2. Alpha tracks viewed under the microscope [10].

2.1.2. Continuous Active Radon Detectors: AlphaGUARD and Airthings. The AlphaGUARD. (Figure 3) is a continuous active radon detector with an ionisation chamber and uses alpha spectrometry for radon detection. The time required for radon diffusion into the ionisation chamber cause a lag in the signal [11]. The device has an internal battery that can operate for roughly ten days. The measurement ranges from 2 Bq/m3 to 2 MBq/m3 with an operating temperature of 10 - 100˚ C. The operating pressure ranges between 700 to 1100 mbar [12]. The working principle of this device is that when radiation passes through gas-filled space or air, molecules get ionised, and a signal is generated [11].

A signal is generated from the alpha detection and converted to a digital output that the computer canread. DataEXPECT software installed in the computer is used to retrieve results from the AlphaGUARD [13]. The Airthings wave radon detector (Figure 4) is a disc sized radon detector operated by a pair of AA batteries. This detector uses a preinstalled three-colour light system to indicate the radon level detected. When the detected radon is high, the light turns red, and it can also beep. The green light indicates low concentration, and the yellow indicates high but not alarming radonlevels. Airthings radon detector uses a smartphone connecting via Bluetooth to download the averageradon concentration and temperature, air pressure, and humidity measured every 60 minutes [14].

Figure 3. AlphaGUARD Professional Radon Monitor [13].

Figure 4. Airthings Waves Radon Detector [14].

2.2. Radon Measurements

The three devices were deployed in the waste room that contains low-level radioactive waste generated from research activities. The study was conducted for three months using active and passive radon measurement techniques. AlphaGUARD had a power supply throughout the exposure period to avoid technical errors due to the instrument switching off. Detectors were placed on top of a shelf approximately 1.5 m above the floor and 150 cm from the wall and door as recommended by the International Atomic Energy Agency (IAEA) [15]. The two active devices also measured the room temperature, pressure, and humidity hourly, corresponding to the measured radon concentration.

However, this study did not focus on these parameters. The measurement interval was set to 60 minutes in both active detectors and measured in Bq/m^3. Microsoft excel data analysis tool was used to analyse the data to obtain the three months indoor radon concentration average (mean). This is a sum of the hourly measured average concentrations divided by the total number of hours of the measurement period (i.e., 245 hours equivalent to 10 days of measurement in the CARST office). The descriptive analysis also gave the minimum, maximum and standard deviation of the data from each active detector. With the passive detector, laboratory analyses (i.e., chemical etching and counting of tracks) was conducted by the supplier (PARC RGM Laboratories). Results were provided as average indoor radon concentration in Bq.h/m^3 and the corresponding standard deviation for the measurement period. The radon concentration was converted to Bq/m^3 by dividing radon exposure in Bq.h/m^3 by 2208 hours, equivalent to the three-month measurement period ([Rn]/Bq/m^3 = Bq.h/m^3/2208 hrs.).

3. Results and Discussions

3.1. CARST Radioactive waste room indoor radon results from the three detectors

Table 1 presents indoor radon levels measured with three devices in the CARST waste room. The three radon detectors were deployed for three months (November 2020 - January 2021). The table also presents the calculated annual effective exposure dose to the students and lecturers at the CARST facility.

According to the ICRP, the reference level of indoor radon is 100 Bq/m^3. Table 1 also indicates that indoor radon concentration levels in the CARST waste room are lower than the recommended levels of 100 Bq/m^3 [16]. Measurements from radon detectors agree with the concentration of 35±18 Bq/m^3 and 37±10 Bq/m^3 from Airthings and the AlphaGUARD radon detectors, respectively. The difference between the two active detectors was expected because they both use the same detection technique. The passive SSNTD measured a radon concentration level of 77±13 Bq/m^3, a level twice that recordedby the active devices. Results show that indoor radon concentration levels in the radioactive waste are below the ICRP recommended reference levels between 100-300 Bq/m^3.

Table 1. Indoor radon concentration levels from the waste room using three different detectors.

Instrument	**Type of measurements**	**^{222}Rn Concentration (Bq/m^3)**	**Standard Deviation (Bq/m^3)**	**Annual Effective Dose (mSv)**
SSNTD	Passive	77	13	0.55
AlphaGUARD	Active	37	10	0.27
Airthings	Active	35	18	0.25

Figures 6 show the fluctuation of radon gas from two active detectors in the waste room. Radon gascan fluctuate hourly, daily and seasonally in the same space, only in 59% of cases where AlphaGUARD results were greater than that of the Airthings. The highest peak observed in figure 6presents a radon concentration of 217 Bq/m^3 by Airthings radon active at 01:31 am on day 52 of the measurements (661 hrs.); at this time, AlphaGUARD measured 53 Bq/m^3. This large difference may be because radon gas does not reach or interact with the detectors simultaneously. This trend is expected since radon gas is not uniformlydistributed and stable in the same space [13].

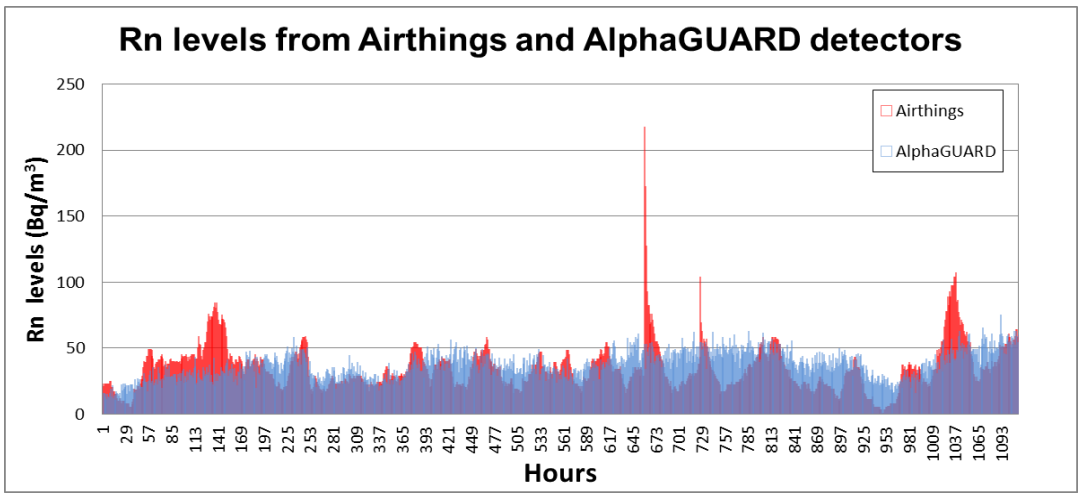

Figure 6. Fluctuations of indoor radon concentration in CASRT radioactive waste room.

3.2. CARST office indoor radon results from the three detectors.

Table 2 presents indoor radon results from a well-ventilated office at the CARST facilities measured with the passive and active detectors. The highest concentration detected from this room is 68±12 Bq/m^3 by SSNTD (Passive) detector. The SSNTD radon concentration in the office is lower than the level measured in the waste room. This may be because the level of radon gas in naturally ventilated environments are always substantially lower than those detected in non-ventilated environments measured by SSNTDs. Indoor radon concentrations measured for two weeks by the two active devices (Airthings and AlphaGUARD) ranged between 10 - 20 Bq/m^3, significantly below the estimated world average of 40 Bq/m^3 [15].

Table 2. CARST office indoor radon concentrations from three different detectors

Instrument	**Type of measurements**	**^{222}Rn Concentration (Bq/m^3)**	**Standard Deviation (Bq/m^3)**	**Annual Effective Dose (mSv)**
SSNTD	Passive	68	12	0.49
AlphaGUARD	Active	12	3	0.09
Airthings	Active	19	11	0.14

The WHO and the IAEA [7, 15] have reported that ventilation is one of the methods to reduce indoor radonconcentrations. This study shows that ventilation plays an important role in indoor radon concentration.A well-ventilated office measured lower radon concentration. Air circulation and ventilation dilute the radon gas after it enters the building. It also reduces the pressure difference between the soil and the occupied spaces, as indicated by the WHO [7].

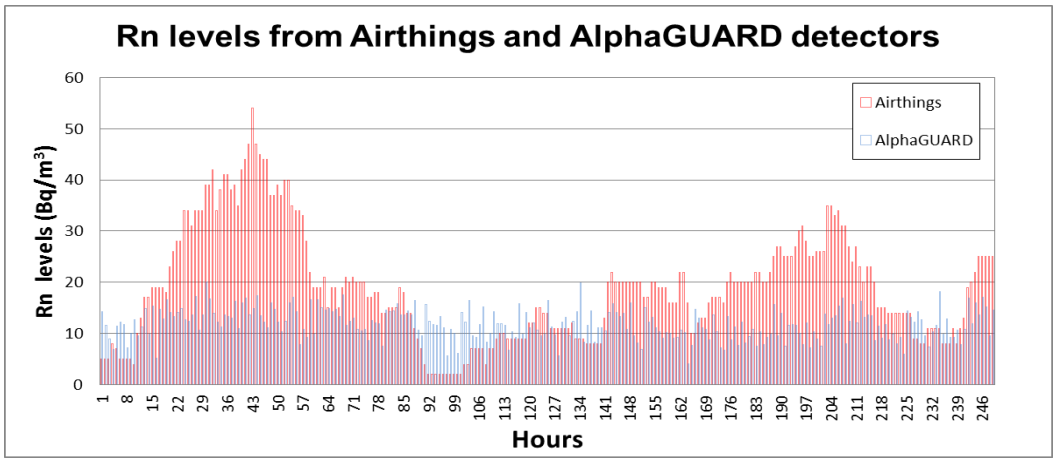

Figure 7. Fluctuations of indoor radon concentration in CARST office.

Figure 7 shows radon gas fluctuation from the two active detectors deployed in the CARST office. AlphaGUARD measured a minimum radon concentration of 4 Bq/m^3 at 23:56 am day 6 of the measurements (165 hrs.). For Airthings, the minimum concentration measured was 2 Bq/m^{3,} and this was constant from 22:56 to 07:56 am on days 3 and 4 of the measurements (93-102 hrs.). The maximum recorded concentration is 54 Bq/m^3 at 08:55 pm (44 hrs.) from Airthings. The maximum concentration measured by the AlphaGUARD is 20 Bq/m^3 at 07:55 am on day 2 of the measurements (31 hrs.).

It has been shown in some studies and reported by the IAEA that indoor radon concentration is higher at night than during the day due to low ventilation because doors and windows are closed. However, from this study, such a trend was not observed. Results show radon concentration variesthroughout; both active detectors measured the maximum and minimum concentrations during the night. In the office, 72% of the time, Airthings results were greater than that of the AlphaGUARD. However, the difference in the average concentrations of the two activedetectors is 7 Bq/m^3 (23%).

Results of the passive detectors deployed in the two rooms (waste room and office) displayed elevated radon concentrations compared to the results of the active detectors. These observations may be attributed to the two techniques operating differently. As mentioned in 2.1.1, AlphaGUARD and Airthings haveionising chambers, and there is a lag/fall back in the detectors because of the time required for radonto get into the ionising chamber to be diffused [13]. SSNTDs are time-integrated detectors with no lag or measurement delays. Another factor that influenced the difference in the measured concentrations is the sensitivity of the instruments.

The low concentration detected by passive detectors (AlphaGUARD and Airthings) could be due tothe fluctuation of atmospheric parameters since both detectors are sensitive to temperature, humidityand air pressure; these parameters; the passive detector (SSNTD) is not sensitive to any meteorological parameters [7]. High temperature, humidity and low air pressure are typicallyassociated with non-ventilated places, resulting in higher radon gas detection. This agrees with the obtained results; the non-ventilated waste room has a higher radon concentration. This is due to the accumulation of radon gas. In the well-ventilated office, temperature and humidity are lower due to air circulation and subsequently reduce the accumulation of radon gas.

The annual effective dose was calculated to get the level that CARST occupants might be exposed to. Active detectors in this study detected the alpha particles from radon in 60 minutes intervals. Theannual effective dose due to inhalation of radon was estimated using the following equation:

$$E_{Rn}\,(mSv.y^{-1}) = DCF_{Rn} \times F_{Rn} \times A_{Rn} \times T_{Rn} \times 10^{-6} \quad (1)$$

Where E_{Rn} is the annual effective dose of inhaled radon, DCF_{Rn} is the radon conversion factor through inhalation (assumed to be 9 mSv/Bqm^{3}h) [17]. F_{Rn} is the indoor equilibrium factor between radon andits progeny (assumed to be 0.4) [18]. A_{Rn} is the radon activity concentration in Bq/m^3, T_{Rn} is the exposure time (assumed to be 2000 hours/yr. for workers).

The estimated annual effective dose calculated from the three devices for the office and waste room is below the ICRP recommended occupational dose limit of 20 mSv/yr. [11, 17]. The calculated annual effective dose in the waste room and office ranged between 0.09-0.55 mSv/yr., below the recommended dose limit. The passive detector measurements indicate that CARST staff and studentsmight be exposed to unsafe doses. However, these results contrast those recorded by active radon monitors, which showed that the calculated effective dose is acceptable.

4. Conclusion

This paper used three different radon detectors to measure radon gas in the waste room and office in two buildings at CARST. Overall results show that there is currently no cause for concern at two CARST buildings due to indoor radon gas. Passive detectors deployed in the waste room and the office recorded a ^{222}Rn concentration above the WHO reported global average indoor radon of 40 Bq/m^3 [9]. The active devices recorded a lower concentration in both the rooms.

The results from active radon detectors in both the waste room are close to each other, with a difference of 2 Bq/m^3 and a larger difference of 7 Bq/$m^{3,}$ which was unexpected. The results obtained from the passive radon detector were relatively higher than those from active detectors in both rooms.From these observations, it can be concluded that the two techniques are different regardless of whether they are in the same room, same exposure time and same environmental parameters, suggesting that one technique must be employed to evaluate the effective dose. The overall indoor radon concentration levels were below the recommended WHO national reference level of 100 Bq/$m^3$and the ICRP recommended radon exposure range of 100-300 Bq/m^3. According to the IAEA and the WHO, the active techniques are excellent for limited surveys, screening and analysing the fluctuation of radon over a short exposure period. Meanwhile, passive techniques are ideal for long-term measurements. They give an overall average radon concentration over a long time. This methodis also excellent for determining the annual effective dose received by the students and CARST staffmembers. However, in this study, it is observed that passive technique Airthings detector agrees with the corresponding standard deviation in both rooms; 35 ± 18 Bq/m^3 and 19 ± 11 Bq/$m^{3,}$ respectively. Airthings radon detector can be trusted and used for long-term and short-term measurements. The use both active and passive detectors for verification purposes. The passive detector is trustworthy because long-term measurements give a good estimate of the radon concentration. Active detectors measured very low concentrations levels that could be representing the backgroundradon.

References

[1] Cothern CR and James JE 2013 *Environmental Science Research*. 35

[2] Moshupya P, Abiye T, Mouri H, Levin M, Strauss M and Strydom R 2019 *Geosciences.* 9(11) 466

[3] Sahu P, Panigrahi DC and Mishra DP 2014 *Journal of Sustainable Mining* 13(3)11-18

[4] Kulali F, Günay O and Aközcan S 2019 International Journal of Environmental Science and Technology. **16**(9)5281-5284

[5] World Health Organization 2001 Evaluation of Carcinogenic Risk to Humans. Ionizing Radiation, part 2: Some Internally Deposited Radionuclides. International Agency for Research on Cancer Press. France

[6] Pule J 2015 South African perspective for radon in dwellings and the anticipated regulatory control measures. SARPA conference. 2015. Villa Paradiso, South Africa: National Nuclear Regulator (NNR)

[7] World Health Organization 2010 WHO guidelines for indoor air quality: selected pollutants

[8] Sethi TK, El-Ghamry MN and Kloecker GH 2012 *Clin Advanced haematology-oncology.* 10(3)157-164

[9] World Health Organization 2009 WHO handbook on indoor radon: a public health perspective

[10] Parc RGM 2021 (Radon gas monitoring) (pty) Ltd, (www.parcrgm.co.za). https://www.parcrgm.co.za/analysis-and-quantification/

[11] Kasar S, Mishra S, Omori Y, Sahoo SK, Kavasi N, Arae H, Sorimachi A and Aono A 2020 *Journal of Soils and Sediments.* 20(1)392-403

[12] Kamunda C, Mathuthu M and Madhuku M 2017 Journal of Environmental and Toxicological Studies. 1(1)

[13] McMurdy., G., *Interfacing the AlphaGUARD Radon Monitor with Campbell Scientific's CR1000 Datalogger*, S. GmbH, Editor. 2009, Campbell Scientific Inc.: Logan, UT p. 753-2342.

[14] Moon B 2019 *Airthings Wave smart radon detector review*. https://blog.bestbuy.ca/smart-Home/airthings-wave-smart-radon-detector-review#.

[15] IAEA 2013 National and regional surveys of radon concentration in dwellings: Review of methodology and measurement techniques

[16] Harrison, J and J Marsh 2020 *ICRP recommendations on radon. Annals of the ICRP*. **49** 68-76

[17] ICRP 2018 ICRP Publication 139: Occupational Radiological Protection in Interventional Procedures

[18] Nader AF 2019 *IOP Conf. Series: Journal of Physics: Conf. Series*, 1258 (2019) 012032

On the advantages of relative phase Toffoli gates

Unathi Skosana[1] and Mark Tame

Department of Physics, SU, Matieland 7602, South Africa

E-mail: [1]unathiskosana@protonmail.com

Abstract. Many of the quantum algorithms that make theoretical guarantees on computational speedups are well beyond the capabilities of currently existing noisy intermediate-scale quantum (NISQ) hardware. The requisite resource demands of these algorithms (*e.g.* qubits, quantum gates, circuit repetitions etc) make their implementation impractical on such hardware. For some algorithms, various approaches exist to reduce these demands. We consider one such approach here. This approach uses relative phase Toffoli gates, advantageous over regular Toffoli gates due to their smaller circuit size. As a proof-of-concept demonstration of the utility of relative phase Toffoli gates, we have used a configuration of these gates in constructing the compiled quantum phase estimation routine to achieve a complete factoring of $N = 21$.

1. Introduction

In classical computation the reversible Toffoli gate is a universal logic gate, *i.e.* any logic circuit L which computes a Boolean function of the form $f : \{0,1\}^n \to \{0,1\}$ can be decomposed into a reversible logic circuit L', equivalent in operation, made up of only Toffoli gates. The truth table and circuit diagram for a Toffoli gate are shown in figure 1.

Inputs			Outputs		
a	b	c	a'	b'	c'
0	0	0	0	0	0
0	0	1	0	0	1
0	1	1	0	1	1
1	0	0	1	0	0
1	0	1	1	0	1
1	1	0	1	1	1
1	1	1	1	1	0

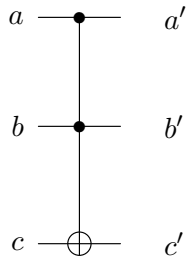

Figure 1. Truth table and circuit for a Toffoli gate.

The reversibility of a Toffoli gate implies that its operation can be realized as a unitary quantum logic gate ($U^{-1} = U^\dagger$), making reversible Boolean arithmetic reproducible on a quantum computer. The Toffoli gate, which is a doubly-controlled NOT (CCX) gate, is described by the following map on a quantum state,

$$\mathrm{CCX}_{abc} : |a, b, c\rangle \mapsto |a, b, c \oplus a \cdot b\rangle \,, \tag{1}$$

where $\oplus$ is modulo 2 addition, $\cdot$ is the bitwise inner product and qubit Hilbert spaces are separated by commas. Notwithstanding their apparent importance, current quantum hardware do not natively support Toffoli gates but rather physically implement a universal gate-set made up of single-qubit gates (*e.g.* $\sqrt{\mathrm{X}}, \mathrm{X}, \mathrm{RZ}$) and a single two-qubit entangling gate (*e.g.* $\mathrm{CX}, \mathrm{CZ}, \sqrt{\mathrm{iSWAP}}$) with high fidelity ($\gtrsim 99\%$ for superconducting qubits, see Ref. [1]). A Toffoli gate is then decomposed into single and two-qubit gates from this native gate-set [2]. Due to the effects of decoherence, there is an upper limit on the number of two-qubit gates over a set of qubits that can be in a circuit, this makes the study of Toffoli gates a subject of interest for practical quantum computing. It has been shown that a three-qubit Toffoli gate (CCX) cannot be implemented with less than five two-qubit gates [3, 4], the traditional three-qubit decomposition into six controlled-NOT (CX) and seven $T/T^\dagger$ gates is shown below

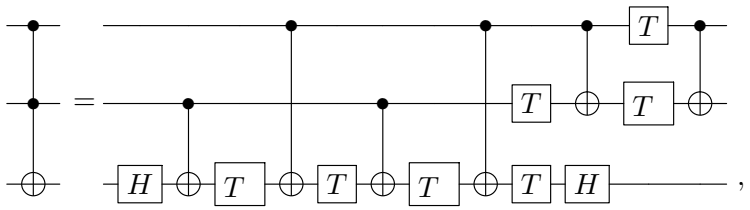

Figure 2. Circuit diagram showing the decomposition of a Toffoli gate in terms of elementary gates; six controlled-NOT (CX) and seven $T/T^\dagger$ gates.

where H is a Hadamard gate and $T = \mathrm{diag}(1, e^{i\frac{\pi}{4}})$. However, there exists variants of the Toffoli gate, smaller in circuit size, collectively called 'relative phase' Toffoli gates due to their operation being equivalent to that of a Toffoli modulo a relative phase shift. Maslov [5] showed that the utility and application of these relative phase variants extends beyond specific and commonly conceived scenarios, leading to a reduction in gate count of known configurations of multiply-controlled Toffolis while preserving functional correctness. Our recently published scheme [6] represents such a specific application of relative phase Toffoli gates, where we employed them for carrying out a demonstration of Shor's quantum algorithm [7] for factoring $N = 21$ on IBM Q's quantum processors. Hence, we introduce the relative phase Toffoli gate and characterize its performance.

2. Generation of entanglement with relative phase Toffoli gates

The relative phase variant which implements a three-qubit Toffoli gate up to a relative shift ($|101\rangle \mapsto -|101\rangle$) is the one considered. The decomposition of such a gate by Margolus [8] , as shown in figure 3, optimally uses three CX gates and four single-qubit gates [9]. We label this gate as RCCX. If in the use of a Toffoli gate such a relative phase shift is permitted, the CX count is significantly reduced in comparison to the full Toffoli shown in figure 2. Consider such an example scenario where we seek to generate entanglement from a state prepared in a three-qubit register:

$$|\psi\rangle = X_0 H_1 \,|0\rangle_0 \,|0\rangle_1 \,|0\rangle_2 = |1\rangle_0 \,|+\rangle_1 \,|0\rangle_2 \,, \tag{2}$$

where X is a bit-flip ($|0\rangle \mapsto |1\rangle$,$|1\rangle \mapsto |0\rangle$) and H is a Hadamard gate ($|0\rangle \mapsto |+\rangle$,$|1\rangle \mapsto |-\rangle$).

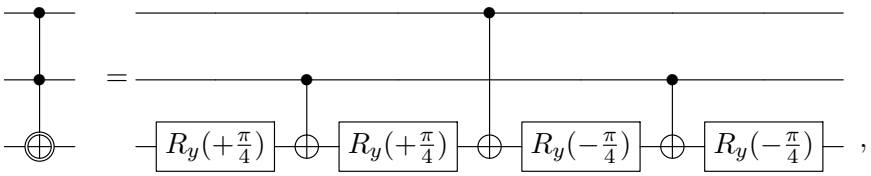

Figure 3. Circuit diagram showing the decomposition of a Margolus gate in terms of elementary gates; three controlled-NOT (CX) and four $R_y(\pi/4)$ single qubit gates, where $R_y(\pi/4) = e^{-i\pi/8}SHTHSZ$,$S = \mathrm{diag}(1, i)$ and $Z = \mathrm{diag}(1, -1)$.

Applying a CCX_{012} to the above state controlled by qubits $0, 1$ and targeted on qubit 2, we produce the state

$$\begin{aligned} \mathrm{CCX}_{012}\left|\psi\right\rangle = \mathrm{RCCX}_{012}\left|\psi\right\rangle &= \frac{1}{\sqrt{2}}\left|1\right\rangle_0\left(\left|0\right\rangle_1\left|0\right\rangle_2 + \left|1\right\rangle_1\left|1\right\rangle_2\right), \\ &= \left|1\right\rangle_0\left|\Phi^+\right\rangle_{12}, \end{aligned} \tag{3}$$

$|\Phi^+\rangle = 1/\sqrt{2}(|0\rangle\,|0\rangle + |1\rangle\,|1\rangle)$ is one of the maximally entangled two-qubit Bell states. In such a scenario, one observes that the state $|101\rangle_{012}$ never arises in the register and thus the operation of CCX and RCCX gates are equivalent. We characterize the performance of these two gates by performing state tomography of qubits 1 and 2 on the state in (3), experimentally prepared on IBM Q's seven-qubit quantum processor *ibmq_casablanca* [10] through the software development kit Qiskit [11]. A typical measured density matrix from the ensemble of measured density matrices is shown in figure 4. To quantitatively evaluate the performance of the two gates in generating the Bell state in (3), we measure the fidelity for two quantum states ρ and σ, defined as $F(\rho, \sigma) = \mathrm{tr}\left(\sqrt{\sqrt{\rho}\sigma\sqrt{\rho}}^2\right)$ [12]. We measured (within 95% confidence intervals) the fidelities to be $F(|\Phi^+\rangle\langle\Phi^+|, \sigma_{\mathrm{CCX}}) = 0.929 \pm 0.003$ and $F(|\Phi^+\rangle\langle\Phi^+|, \sigma_{\mathrm{RCCX}}) = 0.972 \pm 0.008$ for measured density matrices with a CCX and a RCCX gate, respectively. Each measurement performs 8192 circuit repetitions and all other subsequent measurements. The fidelity ranges between 0 and 1, a fidelity equal to 1 means the measured state is equal to the ideal state $\rho = |\Phi^+\rangle\,\langle\Phi^+|$ and fidelity less than 1 indicates how "far away" the state is from ideal. In a larger circuit where more than one Toffoli gate is replaced in such a manner the overall functionality of the circuit would be unaltered, and the difference between the performance of the two gates would be much more discernible.

As further characterization of the two gates concerned, we perform quantum process tomography and reconstruct the χ matrix representation of a quantum channel $\mathcal{E}$ that describes the operation of a circuit. We do this for circuits on the aforesaid quantum processor; *ibmq_casablanca*, which prepared the states shown in figure 4. How closely a quantum channel $\mathcal{E}$ approximates U (the ideal circuit) is described by the average gate fidelity given by:

$$\bar{F}(\mathcal{E}, U) = \int d\psi\, \langle\psi|U^\dagger\mathcal{E}(|\psi\rangle\langle\psi|)U|\psi\rangle\,, \tag{4}$$

where the integration is over the uniform Haar measure on the state space, and $\mathcal{E}(\cdot)$ is an evolution with respect to the quantum channel $\mathcal{E}$. The χ-matrix representation of $\mathcal{E}$ is a matrix χ such that a density matrix ρ under the action of quantum channel $\mathcal{E}$ evolves as such:

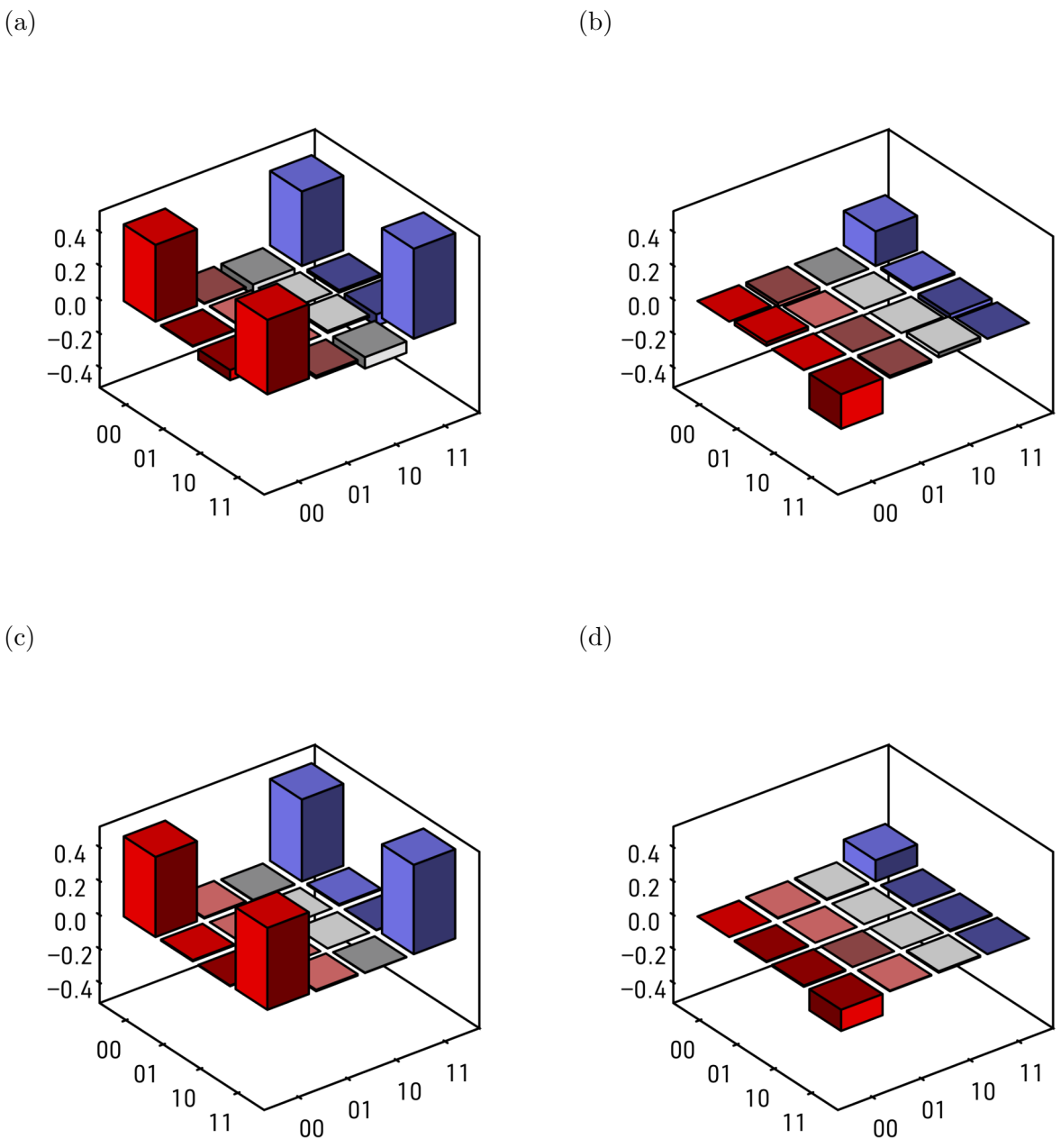

Figure 4. (a) Real and (b) imaginary parts of the measured density matrix of the state of qubits 1 and 2 in (3) prepared with a CCX gate on IBM Q's *ibmq_casablanca*. Similarly, (c) and (d) are real and imaginary parts, respectively, of the same state prepared with a RCCX gate.

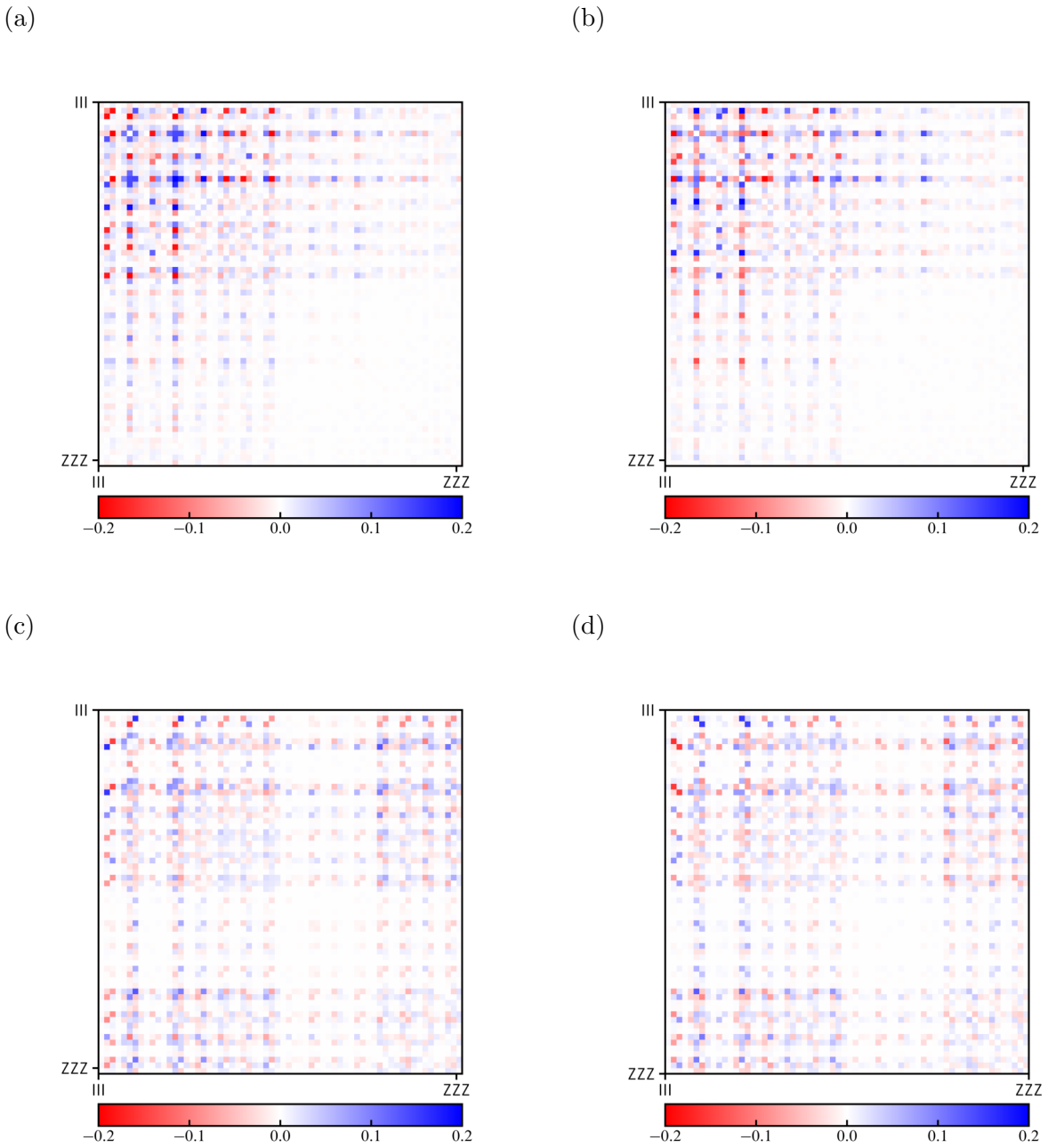

Figure 5. (a) Real and (b) imaginary part of the difference between experimentally measured and the ideal χ-matrix matrix presentation of the quantum channel prepared with a CCX gate on IBM Q's *ibmq_casablanca*, $\mathcal{E}_{\text{ideal}} - \mathcal{E}_{\text{CCX}}$; The largest element differences are 0.254 and 0.322, respectively. Similarly, (c) and (d) are real and imaginary parts, respectively, of the difference the measured and the ideal χ-matrix matrix presentation of the quantum channel prepared with a RCCX gate on IBM Q's *ibmq_casablanca*, $\mathcal{E}_{\text{ideal}} - \mathcal{E}_{\text{RCCX}}$. The largest element differences are 0.163 and 0.163, respectively. In all figures the color bar is rescaled to a range between -0.2 and 0.2 for visual clarity.

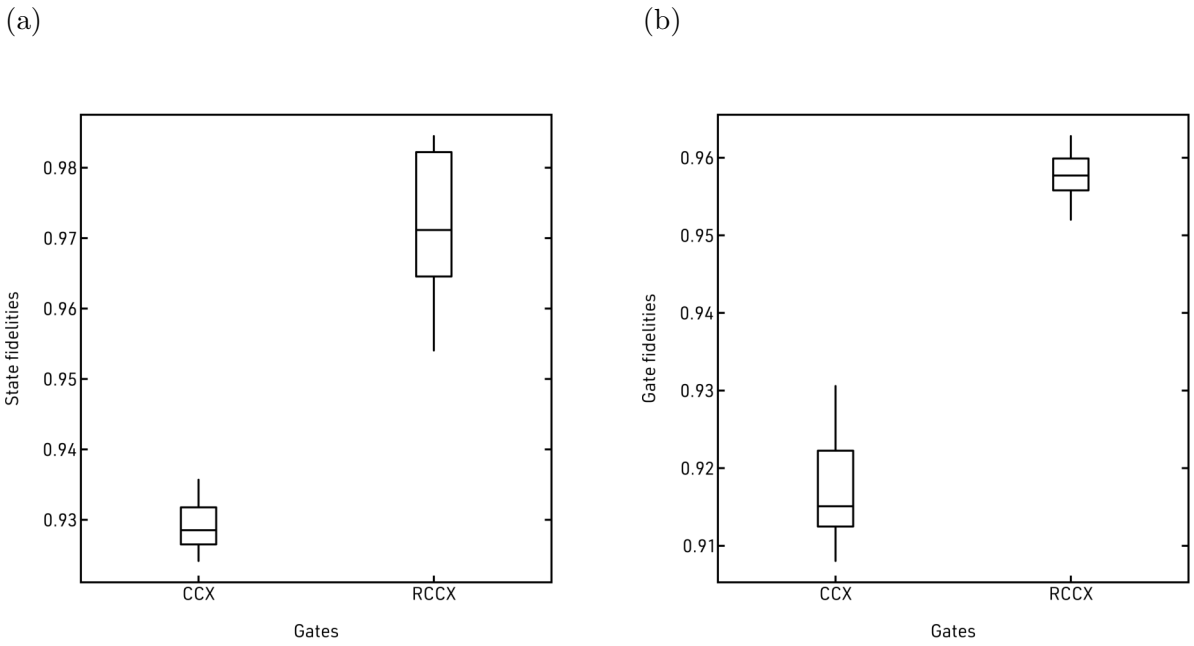

Figure 6. (a) State fidelities between the ideal Bell state $|\Phi^+\rangle\langle\Phi^+|$ and the members of the measured ensemble of density matrices σ_{CCX} and σ_{RCCX} respectively, and (b) average gate fidelities of the quantum channels that prepare the state in (3) with a CCX and RCCX gate respectively.

$$\mathcal{E}(\rho) = \sum_{i,j} \chi_{ij} E_i \rho E_j^\dagger, \tag{5}$$

here the E_i's are n-fold tensor products of all 3^n combinations of Pauli matrices X, Y, Z plus the 2×2 identity matrix I (*e.g.* $E_0 = I \otimes I \otimes I$). See references [13, 14] for closed-form expressions of (4). We measured the average gate fidelities to be $\bar{F}_{\mathrm{CCX}}(\mathcal{E}, U) = 0.917 \pm 0.005$ and $\bar{F}_{\mathrm{RCCX}}(\mathcal{E}, U) = 0.958 \pm 0.002$ respectively, and show differences between the respective measured and ideal χ-matrices in figure 5. In the case of using a RCCX gate, the target unitary preparing the state in (3) is better reconstructed than a CCX gate on the respective processor; the measured χ-matrix for the quantum channel $\mathcal{E}_{\mathrm{RCCX}}$ shows a smaller maximum element-wise difference from its respective ideal χ-matrix than the measured χ-matrix for the quantum channel $\mathcal{E}_{\mathrm{CCX}}$. This is also corroborated by Figure 6, which shows boxplots of state fidelities and average gate fidelities, respectively. We see that comparatively the RCCX gate prepares a Bell state with a higher state fidelity than a CCX gate. Similarly, due to the RCCX gate being comparatively smaller than the CCX gate in terms of its circuit size, it has an overall better average gate fidelity on the IBM Q's *ibmq_casablanca* processor.

3. Relative phase Toffoli gates for quantum factoring

In 2012, the integer $N = 21$ was factored using a small-scale quantum processor, setting the record for the largest integer factored with Shor's quantum factoring algorithm [15]; Similarly in 2019, the integer $N = 21$ was factored again [16]. These two schemes adopt an iterative version of Shor's algorithm which employs a single qubit in the control register that is recycled

through feed forward operations to reduce the qubit overhead of the algorithm. However, at the time of writing, real-time conditional feed forwards operations are not widely supported among current quantum hardware, which the latter implementation [16] circumvented by splitting up the iterations of the algorithm into separate circuits. Moreover, upon further scrutiny, the former implementation [15] fell one iteration short of achieving full factoring.

Building upon the implementation of [15], we identified that Toffoli gates in the algorithm's construction could be replaced with the relative phase Toffoli gate studied here while leaving the operation of the circuit unaltered. As we have seen the latter gate decomposes into fewer elementary gates than the former, and hence improving the fidelity of the output state. As a result, we were able to add a further iteration to the algorithm while maintaining a clear resolution in algorithmic output, from which we were able to successfully extracted the factors of $N = 21$. Our scheme is based on the non-iterative version of Shor's algorithm which uses three qubits for the control register. Notwithstanding the increase in number of qubits in comparison to the aforesaid implementation [15], we were able to successfully factor the integer $N = 21$, and additionally verify the presence of entanglement across the quantum registers in the circuit, See Ref. [6] for details.

4. Summary

Through the use of relative phase Toffoli gates studied in this paper, we were able to go beyond the demonstration of Ref. [15] in fully factoring $N = 21$. In the aforementioned reference, they implemented a compiled and iterative version of Shor's quantum algorithm to factor $N = 21$, and their scheme uses full Toffoli gates to realize Shor's quantum algorithm. Due to this, they were only able to implement two iterations of the algorithm, which falls one iteration short of the minimum number of iterations to be able to extract the factors $N = 21$ from the algorithmic output. Our scheme [6] replaces the full Toffoli gates with relative phase Toffoli gates, while remaining functionally correct (relative phase shifts introduced by gate do not affect the circuit's correctness). This replacement significantly reduces the number of elementary gates in the circuit, allowing our scheme to implement the minimum number of iterations of the algorithm for the full factorization of $N = 21$. We implemented the algorithm on IBM quantum processors using only 5 qubits, successfully verifying the presence of entanglement between the control and work register qubits, which is a necessary condition for the algorithm's speedup in general. Future work in this direction would explore whether the use of relative phase Toffoli gates may be viable in carrying out Shor's algorithm for larger integers, or other algorithms in systems with a limited number of noisy qubits.

Acknowledgments

We acknowledge the use of IBM Quantum services for this work. The views expressed are those of the authors, and do not reflect the official policy or position of IBM or the IBM Quantum team. We thank Taariq Surtee and Barry Dwolatzky at the University of the Witwatersrand and Ismail Akhalwaya at IBM Research Africa for access to the IBM processors through the Q Network and African Research Universities Alliance. This research was supported by the South African National Research Foundation, the South African Council for Scientific and Industrial Research, and the South African Research Chair Initiative of the Department of Science and Technology and National Research Foundation.

References

[1] Kjaergaard M, Schwartz M E, Braumüller J, Krantz P, Wang J I J, Gustavsson S and Oliver W D 2020 *Annu. Rev. Condens. Matter Phys.* **11** 369–395
[2] Barenco A, Bennett C H, Cleve R, DiVincenzo D P, Margolus N, Shor P, Sleator T, Smolin J A and Weinfurter H 1995 *Phys. Rev. A* **52** 3457–3467
[3] Yu N, Duan R and Ying M 2013 *Phys. Rev. A* **88** 010304
[4] Shende V V and Markov I L 2009 *Quantum Inf. Comput.* **9** 461–486
[5] Maslov D 2016 *Phys. Rev. A* **93** 022311
[6] Skosana U and Tame M 2021 *Sci. Rep.* **11** 16599
[7] Shor P W 1997 *SIAM J. Comput.* **26** 1484–1509
[8] Margolus N 1994 *Unpublished manuscript (circa 1994)*
[9] Song G and Klappenecker A 2003 *Quantum Inf. Comput.* **3** 139–156
[10] IBM Quantum 2021 https://quantum-computing.ibm.com
[11] Abraham H *et al.* 2019 Qiskit: An open-source framework for quantum computing
[12] Nielsen M A and Chuang I L 2011 *Quantum Computation and Quantum Information: 10th Anniversary Edition* 10th ed (USA: Cambridge University Press)
[13] Nielsen M A 2002 *Phys. Lett. A* **303** 249–252
[14] Magesan E, Blume-Kohout R and Emerson J 2011 *Phys. Rev. A* **84**
[15] Martín-López E, Laing A, Lawson T, Alvarez R, Zhou X Q and O'Brien J L 2012 *Nature Photonics* **6** 773–776
[16] Amico M, Saleem Z H and Kumph M 2019 *Phys. Rev. A* **100** 012305